

Additive Manufacturing of Lunar Regolith-Stainless Steel Composite Structures

Sierra Green^{1*}

^{1*}Materials Science and Engineering, Massachusetts Institute of
Technology, 77 Massachusetts Avenue, Cambridge, 02139, MA, USA.

Corresponding author(s). E-mail(s): sierragr@mit.edu;

Abstract

This paper explores the development and use of lunar regolith-metal matrix composites fabricated through laser powder bed fusion to increase the lifetime of lunar components, thereby decreasing the demand for lunar resupply launches. LHS-1D is printed on a stainless steel 316 plate in the presence of oxygen to create a surface composite. A wide range of process parameters ranging in energy densities from 8.5-35.7 $\frac{J}{mm^3}$ were studied to determine the effect of laser power and scanning speed on regolith printing. Higher energy densities increase surface roughness, cracking, and balling effects. Lack of fusion and lower adherence of the sample to the build plate is observed in lower energy densities. Best printing results were seen at an energy density of 21-23 $\frac{J}{mm^3}$, however, inconsistencies in spreading the regolith due to the electrostatic attraction between the particles and small particle size make it difficult to quantitatively determine an exact "optimal" parameter range.

Keywords: additive manufacturing, metal-matrix composites, laser powder bed fusion, ISRU

1 Introduction

After recent landing attempts of the Luna-2 and Chandrayaan 3 probes, it is evident that the moon is emerging as an important and increasingly attainable target for mining, geopolitics and human exploration. However, the rapid boom in space exploration seen in the last five years has had a thus-far unrecognized yet increasingly significant carbon footprint. Black carbon and NOx emissions from launch and reentry pose a direct risk to the O_3 layer of the upper stratosphere, and it is estimated increased

launches within the next two decades could cause warming in the upper stratosphere of up to 1.5K/year [1]. As interest in space launches for satellites and rovers or missions geared toward establishing permanent space colonies for mining, scientific pursuit or habitation grows, limiting these launches where possible will become essential to prevent impacting the O_3 layer further. One way to limit such launches is through in situ resource utilization (ISRU), or making use of available lunar resources like moon soil (regolith). This paper evaluates the use of regolith as an ISRU for wear resistant composites, with the goal of creating more durable rover joints to reduce the need for resupply launches to replace or repair broken machinery. ISRUs such as the use of lunar regolith coatings to reduce mechanical wear have the added benefit of making long term habitation more economically feasible as each resupply launch adds cost to a proposed lunar mission.

Due to its prevalence on the lunar surface, regolith has long been identified as a promising resource for lunar habitat construction and as a coating to prevent wear resistance [2],[3], [4]. Since the Apollo missions lunar dust kicked up by Lunar Roving Vehicle activity has been observed to cause increased friction in mechanical parts which leads to shorter lifespan of lunar vehicles [4]. To combat wear caused by this lunar dust, a thin ceramic coating on joints and gears was proposed by NASA [2]. Thus the purpose of this paper is to evaluate the feasibility of printing regolith using laser powder bed fusion (LPBF) on stainless steel surfaces. Through this work a process window for printing thin ceramic coating, which could have future use as a wear resistant composite can be identified, and compared to previous regolith printing efforts and commercial off the shelf coatings.

In a 2023 report for the Lunar Dust Surface Separation Technology Project, Weisner et al. investigated the wear resistance of several commercial off the shelf (COTS) coatings. Taber abrasion tests, sonic wand lunar dust adhesion screening and thermal cycling tests with liquid nitrogen were conducted to determine the wear resistance, adherence of lunar dust and thermal stability of the coatings respectively. the $Cr_3C_2 - NiC$ coating showed the most promise, with a coating loss of less than 2 μm , and resistance to dust adhesion and thermal shock [2]. However, COTS coatings come with inherent disadvantages, namely that significant quantities of ceramic must either be brought along with a lunar habitat for repair and production of new dust resistant parts, or such parts must be manufactured on earth and sent to the habitat every time a replacement is needed. Thus, this paper proposes using lunar regolith itself as a dust resistant coating as it is readily available in lunar environments and has similar CTE, density and composition to the oxides considered in Weisner et al. [2]. The CTE and density for the oxides considered in Weisner et al. [2], Regolith simulants LMS-1D, JSC-1A and KLS1 (a basaltic simulant based on Apollo 14 regolith sample 14163) can be found in table 1[5] [6].

To deposit the regolith surface layer onto the metal substrate, this paper makes use of an additive manufacturing process called Laser Powder Bed Fusion (LPBF). A growing amount of literature has been published on regolith additive manufacturing in the past five years, as interest in using regolith as a construction material for habitats grows with the proposed commercial and governmental lunar settlements. Most literature has focused on the printing of cubes or other 3 dimensional structures for regolith

Table 1 Material Properties of Regolith Simulant and COTS Coatings

Material	Density (g/cm ³)	CTE ($\frac{\mu m}{K}$)
JSC-1A [5]	1.5-1.7	9.5
KLS-1[6]	3.4-3.07	5.0
Exolith Labs LMS-1D [7]	0.79	-
Alumina (Al ₂ O ₃) [2]	3.5	8.3
Alumina-Titania (Al ₂ O ₃ -TiO ₂)	3.5	3.9
Boron Carbide (B ₄ C)	2.53	9.4
Chromium Carbide (Cr ₃ C ₂)	6.68	10.3
Chromium Oxide (Cr ₂ O ₃)	5.22	3.7
Chromium Carbide-Nickel Chrome (Cr ₃ C ₂ -NiCr)	-	6.4
Co-Mo-Cr-Si (Tribaloy T-800)	8.6	-
Stainless Steel 316 [8]	7.87-8.07	15-18

construction as opposed to surface composites as presented in this paper, however, past work gives important insight into substrate selection and laser parameters.

Most printing success has been seen on materials similar to that of the regolith itself such as refractory clay and soda lime glass [9] [10] [11]. Caprio et al. investigated both refractory clay and C40 steel under the same printing parameters and suggested that the inconsistent printing results of the metal was a result of chemical incompatibility, whereas greater success was found with the more chemically similar refractory clay baseplate [9]. Similarly, Goulas et al. conducted an LPBF study using a YAG laser to print regolith on preheated stainless steel 314 and was successful only after applying a proprietary coating which they do not disclose [7]. Goulas et al. also reported cracking due to CTE mismatch between the metal substrate and the regolith, and preheated the baseplate to help alleviate the aforementioned thermal stress. Finally, Iantaffi et al. generated a process window for printing on Al6062, indicating that regolith-metal composites are feasible, if process parameters are correctly optimized [12]

Thus, to correctly achieve regolith printing, process parameter optimization is essential. LMS1-D has been reported to have a sintering temperature between 1100 and 1200°C, which is slightly lower than the sintering temperature for JSC1-A, which is reported at 1280°C by Iantaffi et al. [13] [12]. Thus it is important to note that process parameters will be highly tuned to the composition of the regolith simulant itself, even among papers with similar substrates. This variation may shed light on the wide variety of process parameters which have been successful among literature studies. To evaluate the combined effect of different process parameters on the regolith, energy density is used. Energy density represents the amount of energy deposited in a previously defined amount of the baseplate to sinter the regolith and is a combination of the laser power (W), the laser scan speed(ν), the layer thickness (t) and the distance between two laser tracks, called the hatch distance (h):

$$*E = \frac{W}{\nu th} \quad (1)$$

When the energy density is too high, the regolith vitrifies, or melts, and a phenomenon called balling is observed. With a low energy density, the regolith cannot be sintered to the base plate evenly, resulting in inconsistent printing results. Thus, a process

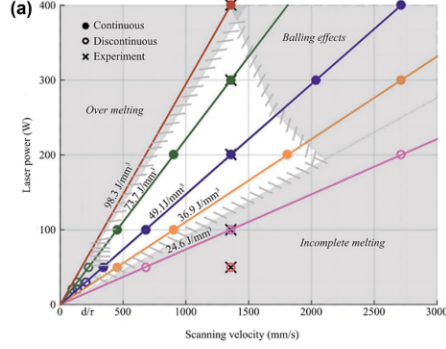


Fig. 1 Process parameter window as presented in Figure 10a) of Iantaffi et al. for JSC1-A on an Al6062 baseplate.

window can be developed for a given regolith simulant on a substrate as shown in a figure by Iantaffi et al. in figure 1 [12].

The goal of this paper is to draw correlations between observed energy density and printing success for a thin regolith layer deposited on a SS316 surface. With this successful printing, a preliminary process window can be created for SS316-regolith surface composites. The paper also employs rehometry and other powder characterization techniques to analyze the stability, specific energy and packing density of the regolith. Wear tests will be conducted to determine the success of this printed regolith layer as a surface composite for resistance to lunar dust.

2 Methods

2.1 Lunar Regolith Simulant

This study makes use of LMS1-D regolith simulant from Exolith labs which is a mixed oxide primarily consisting of SiO_2 , Al_2O_3 , MgO , FeO , and CaO . LMS1-D is meant to simulate the lunar maria dust, and contains a mixture of minerals including glass-rich basalt, bronzite, anorthosite, olivine and ilmenite with an average particle size of $7\mu m$ and a maximum particle size of $30\mu m$ [4] compared with the experimentally measured average lunar dust particle size of approximately $70\mu m$ [3]. A table of LMS-1D composition as compared to lunar regolith and JSC 1-A, another commonly available regolith simulant, is shown in table 2 below. Regolith sample 76501 from the Apollo 17 mission and regolith sample 14163 from Apollo 14 were chosen as comparisons as 76501 is considered representative of lunar highland and high Ti mare basalts, and 14163 is the basis for many commercial samples, including JSC-1A [5] [14].

Table 2 Composition of Regolith Samples

Regolith Type	Particle Size (μm)	Weight Percent (%)									
		SiO_2	TiO_2	Al_2O_3	Fe_xO_x	MgO	CaO	Na_2O	K_2O	MnO	Cr_2O_3
14163 ¹	0-20	48.25	1.6	18.25	9.7	8.9	11.1	0.7	0.57	0.13	0.19
76501 ¹	0-20	41.7	3.3	19.45	11.1	10.45	12.85	0.39	0.11	0.14	0.28
JSC1-A ²	10-1000	47.71	1.59	15.02	10.79	9.01	10.42	2.70	0.82	0.18	0.04
LMS 1-D ³	0.04-35	47.72	2.68	14.02	8.74	14.91	8.26	1.72	0.39	0.18	0

¹Compositional data averaged from 0-10 and 10-20 μm ranges from data found in Table 1 and 4 of Papike et al. respectively. Fe_xO_x contains only FeO. [15]

²Compositional data reported from NASA specification[5]. Fe_xO_x consists of 3.44% Fe_2O_3 and 7.35 % FeO . 0.66% P_2O_5 also reported.

³Compositional data reported from material supplier [14]. Fe_xO_x contains only Fe_2O_3 . 0.20% P_2O_5 also reported.

2.2 Powder Characterization

Before regolith-steel composite samples were printed, the composition, particle size and flowability of the regolith was analyzed. First, particle size was evaluated quantitatively through the Malvern Morphologi 4 system, which takes images of scattered powder to determine the circularity and size distribution of particles. To conduct the test, 15 mL of LMS 1D simulant from exolith labs were injected into the chamber with an injection pressure of 5.0 bar and time of 43 seconds. The particles were imaged at 20x with a height difference of 21 μm to capture different particle sizes and shapes. From these particle images, the circular equivalent diameter (CED), or the diameter of a circular particle with the same area, was calculated using the equation:

$$CED = 2\sqrt{\frac{Area}{2\pi}} \quad (2)$$

This calculation gives an indication of particle size . The circularity was also calculated using the equation:

$$Circularity = \frac{Perimeter}{\pi CED} \quad (3)$$

Circularity varies between 0 and 1, with 1 being a perfectly spherical particle. These results were verified qualitatively via SEM images of particles, and compared with the material specifications. Span index is also presented to analyze the distribution of the particles. Span index is calculated as a ratio between the diameter at the 90th percentile and the diameter of the 10th percentile as shown below, with a larger span index indicating a larger particle size distribution.

$$SpanIndex = \frac{D_{90} - D_{10}}{D_{50}} \quad (4)$$

The composition of the powder was also assessed via EDS analysis, and compared to the material specification.

Next, permeability, compressability, and powder stability tests were performed on an FT4 Rheometer. For the powder stability test, specific energy of the powder is obtained by measuring the work done by moving a blade in an upwards clockwise motion in a 25 x 25 mm vessel. Specific energy (SE) is correlated with the ability of the powder to flow in an unconfined setting (its "flowability"), with a $SE > 10$ mJ/g indicating high cohesion, and an $SE < 5$ mJ/g indicating a low cohesion[16].

The powder stability test also yields a stability index (SI), which is calculated by comparing the specific energy measured from the first test to the energy of the final test to determine if the properties of the powder change as a result of preturbation.

$$SI = \frac{Energy_{Test7}}{Energy_{Test1}} \quad (5)$$

An SI of 0.9;SI|1.1 indicates a stable powder, where as SIs much greater than or less than 1 indicate an unstable powder which indicates particle agglomeration or segregation [16].

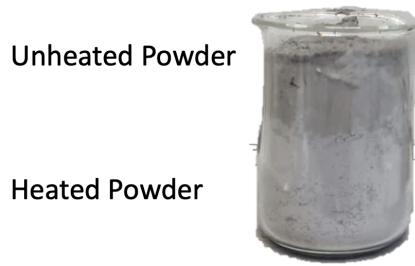


Fig. 2 Exolith LMS 1-D regolith simulant before (top) and after (bottom) heating at 100C for 1 hour.

Compressibility and permeability measurements were also taken to determine conditioned bulk density (CBD). A higher CBD is desirable as these powders are more able to compress without gaps in the substrate. Better filling of gaps (called the packing density) correlates with less porosity in the printed parts. The packing density is expressed as a ratio of the CBD to the bulk density of the powder[16].

Combined, these tests have been used in the past by literature like Cacace et al. and others to analyze the powder's "spreadability." A stable, "spreadable" powder with a higher packing density and good flowability is more likely to spread evenly across the build plate during the recoating step of LPBF [17].

2.3 Spreadability Trials

Spreadability trials were carried out to assess the feasibility of regolith LPBF and determine layer thickness. Similar to the reports from the Apollo missions, the powder was found agglomerate during spreadability tests. This is in contradiction to the powder characterization results, which indicate that the powder by itself is stable. Thus it is concluded that this agglomeration is a result of the low CBD, the presence of electrostatic forces and water retention. It was found that dehydrating the powder for at least 1 hour at 100°C improved spreadability. This was likely due to the dehydration of the powder, and can be clearly seen by the color change between the heated and unheated powder as mentioned in figure 2.

Spreadability tests identified an optimal layer thickness of 0.1 mm for an even coating across the build plate.

2.4 Laser Texturing

Laser texturing was carried out using a pulsed laser from the 3DNT printer. The goal of this was twofold: first, to increase spreadability by providing a nonuniform surface texture which could potentially catch the regolith particles and second, to introduce an oxide layer at the surface of the baseplate which could serve as an intermediate layer between the metal and the ceramic. Laser texturing was carried out in both argon and oxygen, with argon blowing on the oxygen surface to prevent ignition of

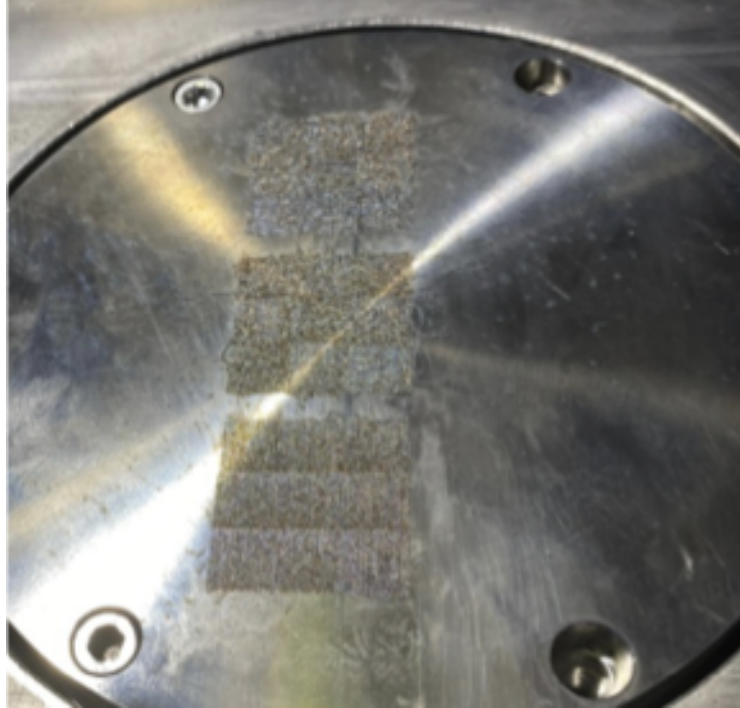


Fig. 3 Laser texturing of the first experiment at the parameters specified above.

the metal. The laser power was set to 500W, with a scan speed of 250mm/s, a hatch distance of 200 μm , a duty cycle of 20%, and a frequency of 0.5 kHz. This resulted in a laser pulse of 400 μs travelling 100 μm of the laser on and 1600 μs travelling 400 μm with the laser off. An image of the laser textured surface can be found in figure 3.

2.5 Printing Conditions

The samples were printed using a 3DNT LPBF machine. In this machine, powder is stored in a hopper to the left of the build plate. During printing, the powder hopper rises to the desired layer thickness, and an automatic recoater blade wipes the powder onto the regolith surface. The 3DNT is equipped with a smart recoater, so images of the powder spreading can be taken during spreadability trials and printing (figure 11). The chamber can be run in oxygen, or in an inert gas such as argon. A diagram of this printer can be found in figure 4. Due to recoating difficulty, the smart recoater was only applied during the "spreadability tests", and tests were done in the presence of oxygen.

Because of the difficulties with spreading the regolith due to electrostatic attraction and particle size, samples were recoated manually by applying a layer of regolith to the surface with a brush. Samples were printed in the presence of oxygen, but with a flow of inert argon onto the samples to create as inert of an environment as possible. Spot size and hatch distance was fixed at 0.07 mm as this was considered an optimum

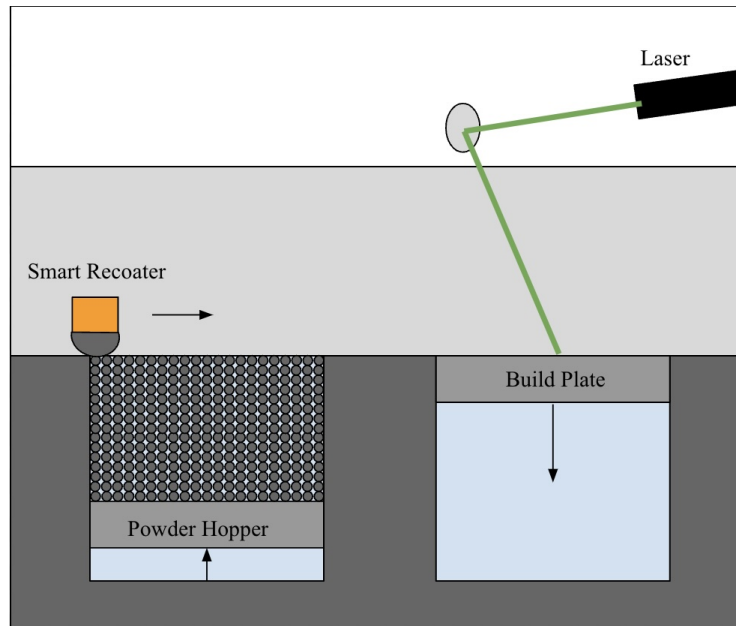


Fig. 4 Schematic of the 3DNT Laser Powderbed fusion printer using the automatic smart recoater.

distance for this printer. Five powers and four scanning speeds were tested on steel base plates for a total of 14 parameter combinations and 12 energy densities to be printed on stainless steel base plates. An additional four parameters were printed on refractory clay base plates in addition to parameters 1, 2.1 and 9.1 as a control. These four additional parameters were taken from Caprio et al.'s successful printing on refractory clay and served as a control to evaluate the impact of powder spreadability on the results [10]. These parameters can be found in tables 3 and 4. These parameters were arranged at random locations on the build plate using the Latin Square approach to account for inconsistencies due to powder agglomeration during recoating and build plate geometry. A sample of this design can be found in figure 4.

2.6 Metallographic Sample Preparation

Cross sections were cut using a band saw and prepared for SEM by hot mounting in pucks of conductive carbon. Samples were then ground and polished following the automatic procedure for stainless steels given in the Buheler grinding and polishing guide, and outlined in the table below[18]. Between polishing steps, samples were sonicated in soap and water for 2 minutes. Before mounting in the SEM, samples were cleaned with acetone. For powder SEM samples, the regolith was placed directly in the SEM without mounting or polishing.

2.7 ImageJ Analysis

Quantitative analysis of oxide layer thickness and coating consistency was conducted using the "Analyze particles" feature of the software ImageJ.

Table 3 Printing Parameters for SS316 Baselplate Trials

Mark Speed (mm/s)	Power (W)				
	156	125	100	75	94
1250		4	8	12	
1000		3	7	11	
750	2.1	2	6	10	
500		1	5	9	9.1

Table 4 Printing Parameters for Refractory Clay Baseplate Trials

Mark Speed (mm/s)	Power (W)				
	156	125	94	55	50
750	2.1	2			
500		1	9.1		
200				L2	L1
225				L4	L3

To measure consistency of the print, stitched color images of the printed samples taken by optical microscope were converted to grey scale. Then a threshold was identified which divided the brighter metal base plate from the darker printed regolith. This threshold was applied 3 times to each image. The command "Analyze particles" was then used to obtain a fraction of light to dark regions, which could be converted into the percentage of regolith that covered the sample.

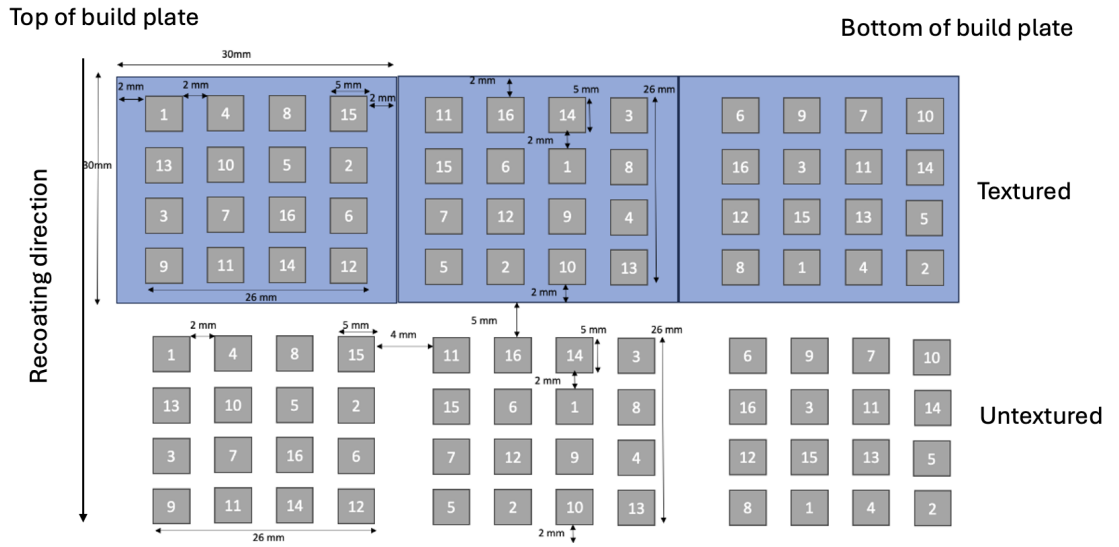


Fig. 5 Build file for initial print with all 12 print parameters arranged in a randomized design based on latin square methodology.

3 Results and Discussion

18 unique parameters varying contour fill, mark speed and laser power were printed on regolith and refractory clay substrates in order to test a wide variety of process parameters for producing successful regolith-steel surface composites. Most success was seen with parameters falling within the energy density range of $21-23 \frac{J}{mm^3}$. Balling was observed in the highest energy density ($35.71 \frac{J}{mm^3}$) and lack of fusion observed in lower energy densities (below $15 \frac{J}{mm^3}$). However, variation in the quantitative ImageJ analysis makes it difficult to unequivocally determine a process window. This variation was likely caused by uneven spreading observed during printing due to the electrostatic attraction between the regolith particles and their small particle size. Thus, future work with larger regolith particle size or different spreading mechanisms is needed to determine the optimal process window to produce regolith-steel composites.

3.1 Powder Characterization

Powder morphology results indicate that the regolith is a fine powder with an average CED of $7.145 \mu m$ and a span index of 1.712. This is close with the exolith particle specification which reports an average particle size of $6 \mu m$, and particle analysis of Exolith Labs LMS 1-D by Millwater et al. which found average particle size to

SumMet method for STAINLESS AND MARAGING STEEL





Surface	Abrasive / Size	Load - lbs [N] / Specimen	Base Speed [rpm]	Relative Rotation	Time [min:sec]
Sectioning	Abrasive Cutter with a wheel recommended for use on ferrous materials HRC35 -50				
Mounting	Compression, typically with EpoMet				
CarbiMet	120 [P120] to 320 grit [P400] SiC water cooled	6 [27]	300		Until Plane
UltraPad	9 μm MetaDi Supreme Diamond*	6 [27]	150		5:00
TriDent	3 μm MetaDi Supreme Diamond*	6 [27]	150		3:00
ChemoMet	0.05 μm MasterPrep Alumina	6 [27]	150		2:00

Fig. 6 Metallographic Preparation of stainless steel samples as recommended by the Buheler guidelines (I will make this into a real table later)[18].

be $7\mu\text{m}$ [19]. Their span index was not reported, however, comparison of the LMS-1D particle size distribution graph given by the material specification sheet and the aforementioned results[14]. A cutoff range of $x < 2.5\mu\text{m}$ and $x > 86.25$ was imposed by the analysis software to differentiate individual lunar regolith particles from shadows or particle clumps respectively. The particle size distribution as a result appears to cut off before the secondary peak at approximately $1.4\mu\text{m}$ reported by the material specification.

Circularity measurements show an mean circularity index of 0.774, which means that the particles are not spherical. Additionally the distribution of particles is quite broad as demonstrated in the figure below, indicating a wide variety of particle morphologies.

This is further corroborated by SEM images of the regolith powder and descriptions of the lunar regolith itself in the Apollo missions. SEM images taken in secondary electron imaging (SEI) mode reveal a non-spherical oxide powder with sharp edges. This morphology is consistent with the SEM images of Exolith Labs LMS and ESA's EAC powder reported in Iantaffi et al, though the powder size of these particles is larger (Iantaffi et al. reported an 50th percentile CED of 56.7 and 60.9 μm for LMS and EAC powders respectively)[12]. Observations of regolith gathered during the Apollo 17 similarly describe the regolith as of a "crystalline" morphology (as opposed to spherical) and indicated a wide variety of particle size, from lunar dust to large rocks[4].

EDS analysis of the regolith indicates a mixed oxide rather than a uniform composition across regolith. This is expected based on the variety in particle size and shape demonstrated above. Chemical analysis of lunar regolith by Papike et al. also indicated a variation of chemical composition with size, with enrichment in $Al - 2O_3$ and trace potassium, rare earth elements and phosphorus (KREEP) for particles $< 10\mu\text{m}$ and MgO enrichment in particles $> 10\mu\text{m}$ [15]. EDS results for Exolith labs stimulant showed a similar trend, with enrichment of FeO and MgO in larger particles. KREEP

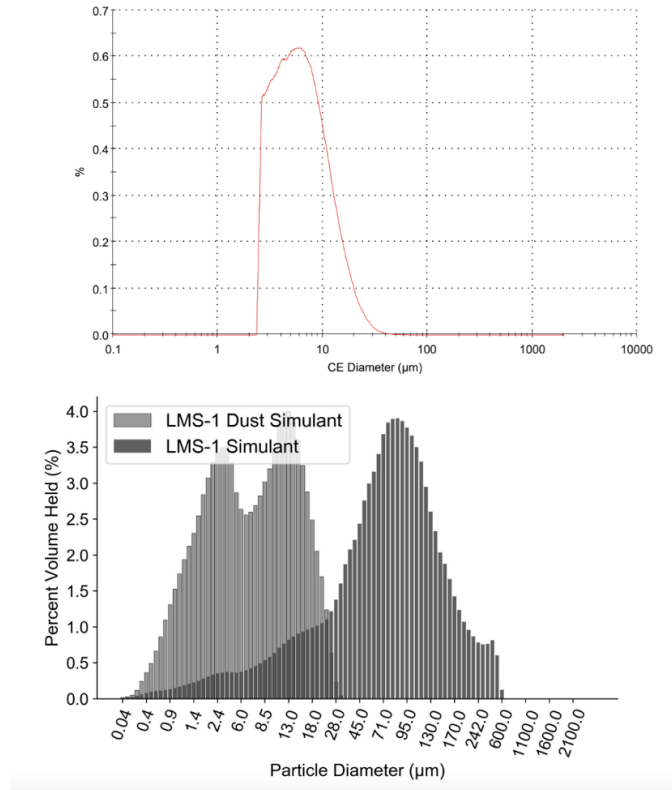


Fig. 7 Results of Morphologi 4 analysis (top) as compared to material specifications (bottom)[14].
 (I need to find a way to overlay these graphs)

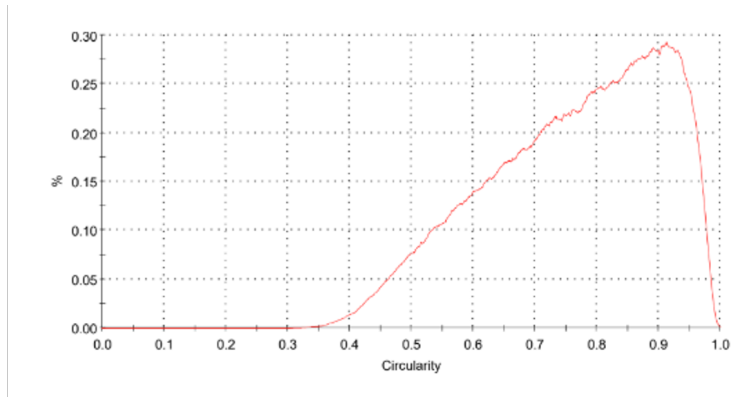


Fig. 8 Volume fraction of regolith particles with a given circularity index.

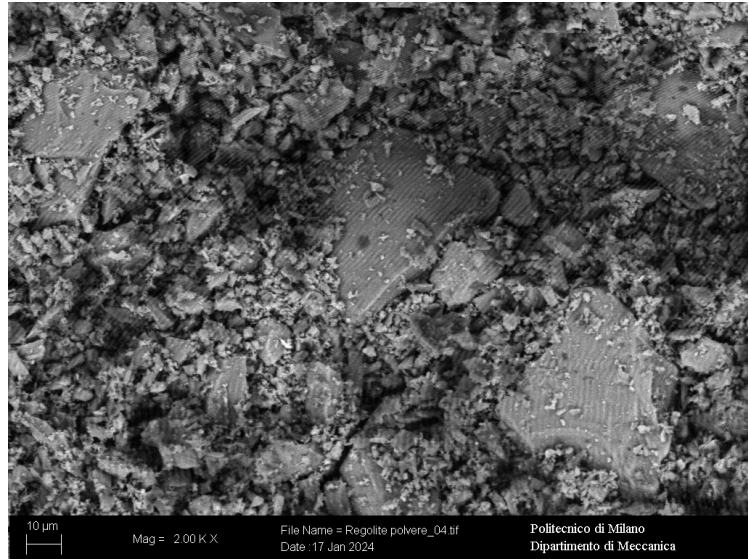


Fig. 9 Regolith simulant LMS1-D from Exolith labs under SEI

Composition by Weight Percent

	SiO ₂	TiO ₂	Al ₂ O ₃	FeO	MnO	MgO	CaO	Na ₂ O	K ₂ O	P ₂ O ₅	Total
Exolith Labs Spec	46.9	3.6	12.4	8.6	0.2	16.8	7	1.7	0.7	0.9	100
2A	38.6	0	0	46.4	0	12.5	2.6	0.0	0	0	100
2B	42.3	0	17.3	12.1	0	8.0	20.4	0.0	0	0	100
6A	47.4	0	0	7.1	0	45.5	0	0.0	0	0	100
6B	50.7	0	34.8	0	0	2.2	12.3	0.0	0	0	100
6C	47.0	0	0	11.8	0	41.3	0	0.0	0	0	100

Image 2:

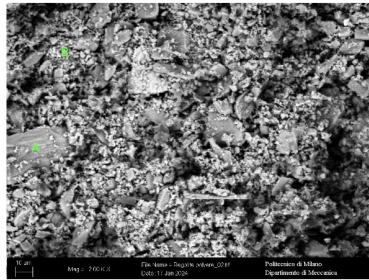


Image 6:

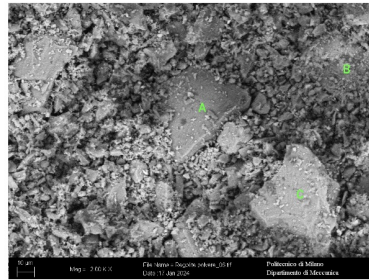


Fig. 10 EDS spots taken from SEM of Exolith labs LMS 1-D regolith simulant shown below.

enriched particles were not detected as evidenced by the lack of P_2O_5 present, though the material specification indicates 0.20 % of P_2O_5 [14]. This could be because the KREEP-y particles were either too small or too well distributed to be detected by the EDS spot scan. Flowability tests with unheated regolith indicate that the powder has an average SE of 12.07 mJ/g across three tests, with a standard deviation of 0.55 mJ/g. As $12.07 > 10mJ/g$, this shows that the particles have a high cohesion. These results align with the observations during the recoating trials that the regolith

Unheated Powder

Heated Powder



Fig. 11 A thin layer of unheated regolith (top) and heated regolith (bottom) spread on a laser textured surface. The unheated powder is darker in color and agglomerates more than heated powder.

tended to agglomerate on the surface of the build plate, rather than evenly coating the surface which can be seen in the figure below. Furthermore, shear measurements by Millwater et al. on Exolith simulants reported a high cohesion in LMS-1D when compared to other Exolith regolith simulants, which they attributed to the smaller particle size of LMS 1-D [19]. It is probable that the cohesion of the particles played a role in the consistency of the print, which resulted in variability of printing results, even when all settings were kept constant.

Powder stability measurements indicated an average stability index of 1.09 across three measurements, with a standard deviation of 0.1. This is inside the range of powder stability ($0.9 < SI < 1.1$), and matches observations that the powder properties did not change with movement due to spreading.

The average CBD as reported from permeability and compressibility tests is 1.07 ± 0.05 and 1.19 ± 0.07 g/mL respectively. This reported CBD is slightly higher than the bulk density reported by Exolith labs of 0.79 g/mL, and that reported by Millwater et al. of 0.78148 ± 0.00634 g/mL [14][19]. This yields a very high packing density of 135.4–150.1%. The packing of the regolith was observed qualitatively during spreading analysis as the dynamic recoater could not be used because it was found to simply compress the regolith in the powder repository section rather than spreading it across the build plate.

3.2 Energy Density for Metal Printing

This paper was unable to establish a definitive trend between energy density and regolith printing due to inconsistencies in powder spreading as discussed above. Optical analysis via ImageJ indicated variation in average regolith coverage from sample

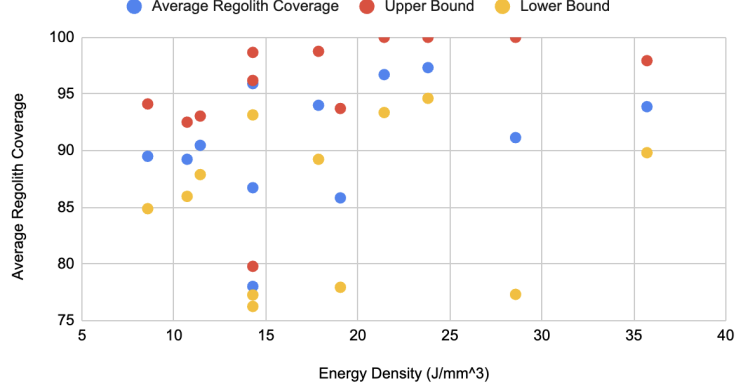


Fig. 12 Average regolith coverage versus energy density as measured by ImageJ analysis of optical micrographs.

to sample, depending on location within the build plate and regolith spread. The middle of the build plate had the most consistent printing, which matches with known expectations about additive manufacturing. A graph of average regolith coverage versus energy density can be found in figure 12. While it is difficult to establish an exact process window, the highest average regolith coverage was found in samples 2 and 9, with energy densities of $23.81 \frac{J}{mm^3}$ and $21.43 \frac{J}{mm^3}$ respectively.

These energy densities are much higher than the $1.49 \frac{J}{mm^3}$ energy density reported most successful by Iantaffi et al. [12]. However this lower energy density value is due to a one magnitude difference in hatch distance, rather than scanning speed and laser distance, which was not a parameter varied in this paper. Iantaffi et al. reported a hatch distance of 0.25mm whereas these experiments were conducted with a hatch distance of 0.07mm as this was found to be optimal for the 3DNT printer. When comparing laser powers, Iantaffi et al. found a power of 145W most successful when coupled with a rescan at 102W, compared with the 125 W and 94 W used by this parameter 2 and parameter 9. However, Iantaffi et al. used a lower scan speed of around $390 \frac{mm}{s}$ as opposed to $750 \frac{mm}{s}$ and $500 \frac{mm}{s}$ used in parameters 2 and 9 respectively.[12] Thus while this paper’s work reaffirms that a range from 100-145W seems to be optimal for regolith sintering, future experiments need to be done with more consistent recoating to provide clearer results. Furthermore, future work varying hatch distance is essential to understand the effect of this parameter on regolith printing success.

Similar to the process parameter window seen in figure 1, higher energy densities showed balling and greater spattering of the metal, while lower energy densities exhibited patchiness and a more uniform surface roughness. In figure 13, balling is seen in parameter 1, which had the highest energy density of $35.714 \frac{J}{mm^3}$. Balling is caused by vitrification of the regolith, and creates a rough surface that makes further layering difficult, thus it is not desired for surface composites that need a smoother surface. On the other hand, the steel consistently appears in patches in the lower energy densities ($E < 11.429 \frac{J}{mm^3}$). This is likely because the energy density is not high enough to fully melt the regolith, resulting in lack of fusion. Lack of fusion can also be seen even among samples with higher energy densities, but to a less severe degree as the

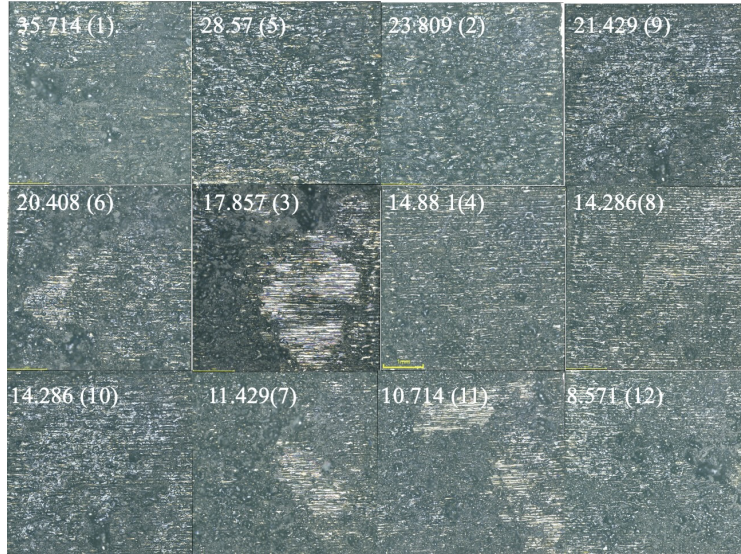


Fig. 13 Top view of regolith-steel composites organized by energy density.

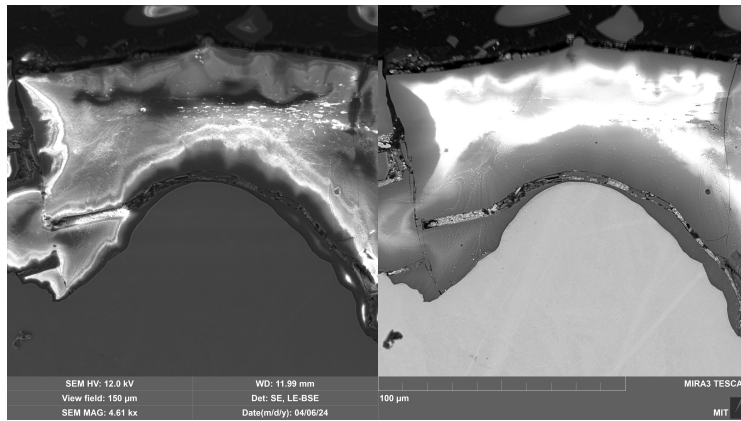


Fig. 14 Secondary electron (left) and backscatter image (right) of regolith-steel composite printed with parameter 9.1. Lack of fusion is seen in the crack in the backscatter electron image.

regolith coating remains adhered to the sample. Cross sectional analysis of parameter 9.1, with an energy density of $26.57 \frac{J}{mm^3}$ which is closer to the energy range of 21-23 $\frac{J}{mm^3}$ identified as most optimal by this paper, also showed a much smoother surface, with less spattering of steel and balling than can be seen the cross section of parameter 1, which had a higher energy density of $35.714 \frac{J}{mm^3}$ in figure 16.

Therefore, though it is difficult to discern a definitive optimal range of process parameters until spreadability is improved, SEM and ImageJ analysis indicate that lower scan speeds of 500 and 750 $\frac{mm^2}{s}$ and powers between 100-125 $\frac{J}{mm^3}$ show greater regolith covering, without balling, and limited patchiness.

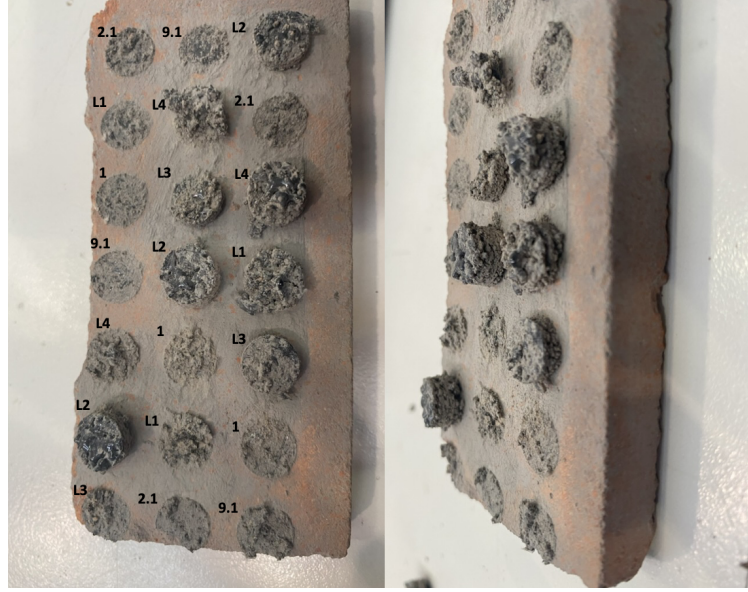


Fig. 15 Top view (left) and side view (right) of regolith simulant LMS1D printed in cylinders on refractory clay.

3.3 Base Plate Effects

Despite inconsistencies due to spreading, it is clear that metal base plates require higher laser power and scan speed for successful printing. In this paper, experiments were carried out on refractory clay base plates comparing the metal parameters 2.1, 1 and 9.1 (with powers ranging from 94-156 W and scan speeds of $500-750 \frac{mm}{s}$), which showed some success on metal to parameters L1-L4 (powers of 50-55W and scan speeds of $200-225 \frac{mm}{s}$) which were successful in Caprio et al. [9]. As seen in figure 12, the only the lower power samples (L1-L4) exhibit growth in the z direction, whereas higher power parameters (2.1,1,9.1) exhibit vitrification and balling effects. This is the opposite from the trend observed for the SS316 base plate presented in figures 12 and 13 which show lower average regolith coverage and increased lack of fusion with lower powers.

Thus, it can be concluded that sintering at lower power and scan speed is better for ceramic. This is likely due to the similar chemical composition and coefficient of thermal expansion between the refractory clay base plate and the regolith. By weight, LMS1D regolith simulant is 61.74% SiO_2 and Al_2O_3 , which are the two components in refractory clay. Thus, it is easier for the regolith to adhere to the oxide, due to the similarity in both bonding type and CTE between these structures. Conversely, the SS316 base plate has a CTE of $15-18 \frac{\mu m}{K}$ which is much larger than the reported CTE range of $5-9.5 \frac{\mu m}{K}$ for regolith simulants. Thus, it is more difficult to bond to the metal both because the molten regolith does not wet the surface due to differences in chemistry, but also because residual thermal stresses caused by CTE mismatch cause cracking upon solidification of the regolith. Furthermore, regolith has a sintering

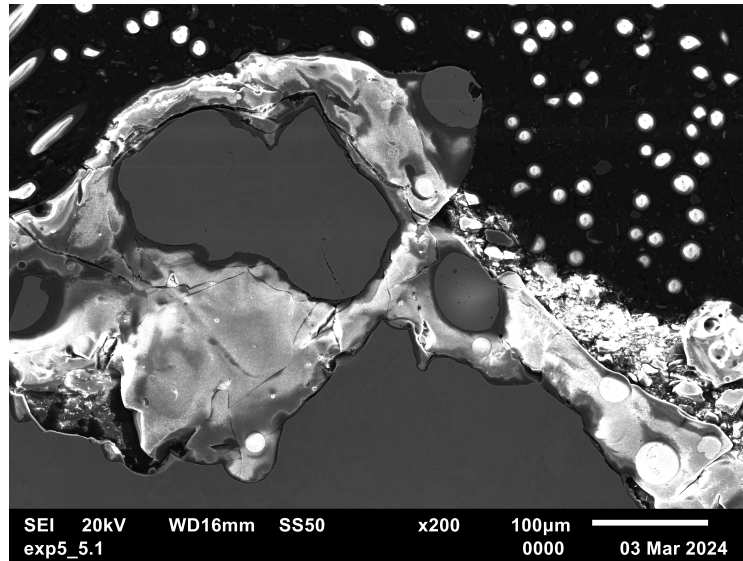


Fig. 16 A secondary electron image of a cross section of a regolith-steel composite printed using parameter 1.

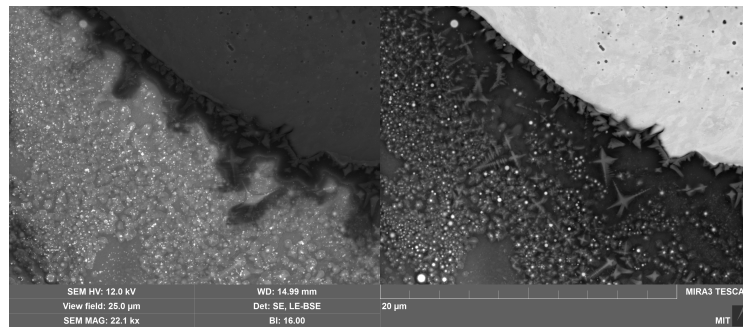


Fig. 17 Secondary electron (left) and backscatter (right) image of dendrites forming in the regolith melt of a regolith-steel composite printed with parameter 1.

temperature of around 1280 ° C whereas steel has a melting temperature of 1375-1400 ° C [12] [8].

At higher laser powers, the steel underneath the regolith melts and fragments break off and mix with the regolith as can be seen in figure 13. This increases the interaction between the regolith and the steel, as molten regolith becomes trapped under melted and resolidified sections of steel. Furthermore, the cooler, resolidified steel droplets act as nucleation sites for regolith solidification. This can be seen in figure 14 below, where dendrites form in the regolith melt pointing away from the steel particle.

The trend that higher power needed for regolith printing on metal baseplates is also observed in the work done by Iantaffi et al. which identified a power of 145 W as the optimal printing parameter for Al6062 [12]. Iantaffi et al. also found that a rescan

strategy at a lower power of 100W after the first layers are printed increases print success, which similarly matches the conclusion of this paper that a lower power is preferable to bind the regolith to itself or another oxide.

4 Conclusion

In conclusion, continued optimization of the printing process and setup is essential before regolith-steel composites can be produced for wear testing. Though this paper did show the first preliminary successful printing results of printing regolith directly to uncoated steel, inconsistent spreading of the regolith due to electrostatic attraction of the particles and a small particle size made it difficult to firmly determine an optimal process window for printing. Future work with a larger particle size such as that used by Caprio et al. or Iantaffi et al. could yield more consistent spreading, and therefore more consistent results. [9] [12] Furthermore, it is determined that higher power is needed to adhere the regolith to the metal build plate, while lower powers are better for sintering the ceramics together, and printing the regolith layers. This would explain why Caprio et al. saw success on refractory clay but not with steel, as they were conducting experiments at 50-55 W as compared to the 156-75 W considered in this experiment. Future work on a "graded power composite" which starts at a higher power to adhere the regolith to the build plate in the first few layers, and transitions to a lower power once a consistent regolith layer is achieved to continue growth in the vertical direction could yield more successful composites with higher vertical growth. Once regolith composites can be reliably synthesized within an optimal parameter window, Taber or continuous wear tests using SiC paper should be conducted to determine the abrasion resistance of the sintered regolith composite. If three dimensional samples can be produced, compression tests can also be done, and compared to compression tests carried out by others in literature including Caprio et al. and Goulas et al. [9] [5]. Through this work, it has been proven that regolith can be successfully printed in a thin layer on a SS316 surface, though further work in improving the consistency and quality of these layers is essential before mechanical testing can be undertaken. This paper provides a foundation and preliminary successful results as a small step toward a greater innovation in regolith-metal composite structures, and sustainable space exploration.

Acknowledgements. Contribution to the printing, powder analysis and results were made by Stefania Cacace, Alessandro Margharita, and Leonardo Caprio. SEM images were taken with help from Parth Khandelwal. Cem Tasan and Bianca Maria Colossimo assisted with the technical advising of this project. Caroline Beimford and Elsa Olivetti provided guidance in the writing of this draft.

References

- [1] Maloney, C.M., Portmann, R.W., Ross, M.N., Rosenlof, K.H.: The climate and ozone impacts of black carbon emissions from global rocket launches. *Journal of Geophysical Research: Atmospheres* **127**(12), 2021–036373 <https://doi.org/10.1029/2021JD036373>

<https://agupubs.onlinelibrary.wiley.com/doi/pdf/10.1029/2021JD036373>.
e2021JD036373 2021JD036373

- [2] Wiesner, W.C.J.K.G.C. Valerie, Jordan, K.: Protective coatings for lunar dust tolerances. NASA STI program (April 2023)
- [3] Stubbs, T., Vondrak, R., Farrell, W.: Impact of dust on lunar exploration. *Dust in Planetary Systems*, 239–243 (2007)
- [4] Goodwin, R.: *Apollo 17: The NASA Mission Reports vol. 1*. Apogee Books, Ontario, Canada (2002)
- [5] McKay, D.S., Carter, J.L., Boles, W.W., Allen, C.C., Allton, J.H.: JSC-1: A New Lunar Regolith Simulant, 963 (1993)
- [6] Kim, Y.-J., Ryu, B.H., Jin, H., Lee, J., Shin, H.-S.: Microstructural, mechanical, and thermal properties of microwave-sintered kls-1 lunar regolith simulant. *Ceramics International* **47**, 26891–26897 (2021) <https://doi.org/10.1016/j.ceramint.2021.06.098>
- [7] Goulas, A., Friel, R.: 3d printing with moondust. *Rapid Prototyping Journal* **22**, 864–870 (2016) <https://doi.org/10.1108/RPJ-02-2015-0022>
- [8] Properties: Stainless steel. AZO Materials (2001)
- [9] Caprio, L., Demir, A.G., Previtali, B., Colosimo, B.M.: Determining the feasible conditions for processing lunar regolith simulant via laser powder bed fusion. *Additive Manufacturing* **32**, 101029 (2020) <https://doi.org/10.1016/j.addma.2019.101029>
- [10] Goulas, A., Binner, J.G., Engstrøm, D.S., Harris, R.A., Friel, R.J.: Mechanical behaviour of additively manufactured lunar regolith simulant components. *Proceedings of the Institution of Mechanical Engineers, Part L: Journal of Materials: Design and Applications* **233**(8), 1629–1644 (2019) <https://doi.org/10.1177/1464420718777932>
- [11] Koike, R., AlKhaled, A., Kashimoto, T.: Basic study for lunar regolith powder bed fusion in high gravity. *CIRP Annals* **72**(1), 125–128 (2023) <https://doi.org/10.1016/j.cirp.2023.04.022>
- [12] Iantaffi, C.: Additive manufacturing for lunar in situ resource utilization. PhD thesis, University College London (2023)
- [13] Warren, P., Raju, N., Ebrahimi, H., Krsmanovic, M., Raghavan, S., Kapat, J., Ghosh, R.: Effect of sintering temperature on microstructure and mechanical properties of molded martian and lunar regolith. *Ceramics International* **48**(23, Part B), 35825–35833 (2022) <https://doi.org/10.1016/j.ceramint.2022.07.329> .

- [14] Exlolith Labs: LHS-1D Dust Simulant Fact Sheet. (2023). Exlolith Labs. Batch 8/15/2023-4/7/2024
- [15] Papike, J.J., Simon, S.B., Laul, J.C.: The lunar regolith: Chemistry, mineralogy, and petrology. *Reviews of Geophysics* **20**(4), 761–826 (1982) <https://doi.org/10.1029/RG020i004p00761>
<https://agupubs.onlinelibrary.wiley.com/doi/pdf/10.1029/RG020i004p00761>
- [16] FT4 Powder Rehometer User Manual. Freeman Technologies
- [17] Cacace, S., M.Boccardo, Semeraro, Q.: Investigation on the effect of the gas-to-metal ratio on powder properties and pbf-lb/m processability. *Progress in Additive Manufacturing* (2023)
- [18] Grinding and Polishing Guide. Buehler
- [19] Millwater, C., LongFox, J., Landsman, Z., Metke, A., Britt, D.: Direct Shear Measurements of Lunar Regolith Simulants LHS-1, LHS-1D, LMS-1, and LMS-1D (2022)